HHS Public Access

Author manuscript

Nat Methods. Author manuscript; available in PMC 2014 January 01.

Published in final edited form as:

Nat Methods. 2013 July ; 10(7): 653–658. doi:10.1038/nmeth.2488.

Video-rate nanoscopy enabled by sCMOS camera-specific single-molecule localization algorithms

Fang Huang[1], **Tobias M. P. Hartwich**[1,2,3,9], **Felix E. Rivera-Molina**[1,9], **Yu Lin**[4,5], **Whitney C. Duim**[1], **Jane J. Long**[6], **Pradeep D. Uchil**[7], **Jordan R. Myers**[1], **Michelle A. Baird**[8], **Walther Mothes**[7], **Michael W. Davidson**[8], **Derek Toomre**[1], and **Joerg Bewersdorf**[1,4,5,*]

[1]Department of Cell Biology, Yale University School of Medicine, New Haven, CT 06520, USA

[2]Department of Biophysical Chemistry, University of Heidelberg, 69120 Heidelberg, Germany

[3]Department of New Materials and Biosystems, Max Planck Institute for Intelligent Systems, 70569 Stuttgart, Germany

[4]Department of Biomedical Engineering, Yale University, New Haven, CT 06520, USA

[5]Integrated Graduate Program in Physical and Engineering Biology, Yale University, New Haven, CT 06520, USA

[6]Yale College, Yale University, New Haven, CT 06520, USA

[7]Department of Microbial Pathogenesis, Yale University School of Medicine, New Haven, CT 06520, USA

[8]National High Magnetic Field Laboratory and Department of Biological Science, Florida State University, Tallahassee, FL 32310, USA

Abstract

Newly developed scientific complementary metal–oxide–semiconductor (sCMOS) cameras have the potential to dramatically accelerate data acquisition in single-molecule switching nanoscopy (SMSN) while simultaneously increasing the effective quantum efficiency. However, sCMOS-intrinsic pixel-dependent readout noise substantially reduces the localization precision and introduces localization artifacts. Here we present algorithms that overcome these limitations and provide unbiased, precise localization of single molecules at the theoretical limit. In combination with a multi-emitter fitting algorithm, we demonstrate single-molecule localization super-

*Correspondence to: Joerg Bewersdorf joerg.bewersdorf@yale.edu.

[9]These authors contributed equally to this work

AUTHOR CONTRIBUTIONS

F.H. and J.B. conceived the project. F.H., T.M.P.H., Y.L. and J.B. built the setup and designed the bead experiments. All authors designed the biological imaging experiments. F.H., T.M.P.H., Y.L., J.J.L., P.D.U. and J.R.M. performed the fixed cell experiments. F.H., F.E.R.-M., W.C.D. and J.J.L. performed the live cell experiments. M.A.B. and M.W.D. generated the mEos3.2 and tdEos plasmids. F.H. wrote the software and performed the simulations and analysis. All authors wrote the manuscript.

COMPETING FINANCIAL INTERESTS

F.H. and J.B. are co-inventors on a patent application related in part to the material presented here. J.B. is consultant, equity holder and member of the scientific advisory board of Vutara, Inc., which makes super-resolution microscopes.

resolution imaging at up to 32 reconstructed images/second (recorded at 1,600–3,200 camera frames/second) in both fixed and living cells.

SMSN techniques localize single molecules with precisions in the 10-nm range by stochastically switching them on and off.[1–3] Thousands (or even tens of thousands) of camera frames of blinking subsets of molecules are typically recorded to obtain a single image at about 25–40 nm resolution. The temporal and spatial resolutions are limited by several factors: the number of photons emitted by a single molecule per frame, and the sensitivity (quantum efficiency) and readout speed of the camera.

Until now, back-illuminated electron-multiplying charge coupled devices (EMCCD) have been the predominantly used cameras in SMSN due to their low effective readout noise achieved by electron multiplication. However, the noise introduced by the amplification process results in a decrease in the signal-to-noise ratio by a factor of ~$2^{1/2}$,[4] and effectively halves the high quantum efficiency (~95%) of these sensors to < 48%[4] unless each pixel detects generally less than one photon on average[5]. At the same time, the readout speed of 512 × 512 pixel EMCCD cameras is currently limited to 70 full frames/s (fps). Typical acquisition times of SMSN using these cameras range from minutes up to an hour. Since the first realization of live-cell imaging with these techniques,[6] an especially important goal has been to improve this speed. To increase the camera frame rate to several hundred fps, readout can be limited to smaller regions of interest (ROIs) of the chip or cameras with fewer pixels can be used (for example 128 × 128 pixels). This has enabled live-cell SMSN of photoswitchable fluorescent proteins with a temporal resolution of several seconds to tens of seconds, and down to 500 ms using organic fluorophores[7,8]. However, the accessible field of view (FOV) is usually severely compromised for temporal resolutions in the 1-s range.

This trade-off between imaging speed and FOV has so far substantially limited the capabilities of SMSN to address practical biological questions: many biological phenomena are either so rare that imaging only small FOVs is highly inefficient, or the phenomena are best interpreted in the larger context of the cell (requiring imaging of large FOVs). This problem is of even greater concern when considering the application of SMSN to high-throughput screening approaches. The trend towards systematic and quantitative analysis of cellular systems as represented by the increasing number of 'omics' techniques has not been expanded to nanoscopy, mainly because high recording speeds of large FOVs have been lacking. This has so far impeded the application of nanoscopy techniques to systematic studies of complex cell biological processes.

Recently, scientific complementary metal–oxide–semiconductor (sCMOS) cameras have been introduced that feature an effective quantum efficiency of up to 73% at a wavelength of 600 nm, a large FOV (> 2,000 × 2,000 pixels) and much faster readout speeds than EMCCD cameras. These advantages can potentially benefit both the localization precision and temporal resolution of nanoscopes, making sCMOS devices attractive alternatives to EMCCD cameras. Unfortunately, the architecture of sCMOS cameras results in every pixel having a unique noise characteristic. For example, the noise variances of individual pixels range from several ADU^2 (analog to digital units) to thousands of ADU^2 (Fig. 1a and Supplementary Fig. 1).

It has been recently demonstrated that single-molecule localization and super-resolution imaging are feasible with sCMOS cameras[9,10]. However, due to the non-negligible, pixel-dependent noise of sCMOS cameras, the used single-molecule localization algorithms which were originally designed for EMCCD cameras[4,11,12] fail to provide reliable position estimates as the underlying noise model is no longer Poisson distributed and pixel independent.

To illustrate this problem, we simulated recorded camera frames based on a test structure consisting of two parallel lines and included pixel-dependent variations in the readout noise and gain typical for sCMOS cameras (Fig. 1b and Online Methods). The simulated frames were then analyzed with a conventional maximum-likelihood estimation (MLE) algorithm which has been demonstrated to perform at the Cramér-Rao lower bound (CRLB) limit with EMCCD data[12]. The two lines erroneously merge in the vicinity of a pixel with high readout noise (Fig. 1b), clearly demonstrating that the application of conventional localization methods leads to inaccurate reconstructions when applied to sCMOS data sets.

Here we overcome this problem by applying a new set of algorithms that include the observed noise behavior of sCMOS cameras in the localization process. This approach allows unbiased and precise localization analysis with sCMOS cameras. In contrast to conventional localization methods, we model noise as a combined probability distribution of Poisson-distributed shot noise and Gaussian-distributed pixel-dependent readout noise. The new noise model is consistently applied to all of the steps – image segmentation (IS), single-molecule localization, fit rejection and uncertainty estimation – required for super-resolution analysis (Supplementary Fig. 2).

To accurately model the pixel-dependent noise behavior, careful characterization of the amplification gain, the Gaussian noise variance, and the offset of every pixel of the sCMOS camera is required. For this purpose, we carefully characterized our sCMOS camera (ORCA Flash 4.0, Hamamatsu Photonics) and determined the mean ('offset'), the variance and the amplification gain of each pixel (Online Methods; Fig. 1a).

With this information, unbiased and precise single-molecule localization analysis can now be performed. In the first step, IS, candidates for single-molecule localization are identified in the raw data. We have adapted commonly used smoothing filters[13] for this purpose by statistically weighting the information from each pixel by its inherent variance and gain (IS_{sCMOS}; Supplementary Note). This approach successfully eliminates large noise peaks in the smoothed images caused by noisy pixels, which could otherwise be interpreted as single molecules.

In the following localization step, molecule positions are estimated for the identified candidates. Here, we have implemented our new sCMOS noise model in the likelihood function of the MLE framework (Supplementary Note). Consideration of the noise and gain inherent to each pixel requires that the likelihood function is based on a probability distribution described by the convolution of the Poisson-distributed photon shot noise with the pixel-dependent Gaussian noise distribution. However, this convolution must be computed for each pixel during every fitting iteration, a prohibitive step due to the

overwhelming computational complexity. We have solved this problem in our localization algorithm, MLE_{sCMOS}, by introducing an analytical approximation that greatly simplifies the calculation while providing optimal accuracy and precision at the theoretical limit (Fig. 1c,d, Supplementary Fig. 3, Supplementary Note).

Additionally, to correctly identify and eliminate non-converging fits and fit errors, we have developed a goodness of fit test based on a log-likelihood ratio metric (Supplementary Note). The new algorithm, LLR_{sCMOS}, uses the sCMOS camera noise model and its approximation introduced above. The metric follows a χ^2-distribution as expected from theory and thus allows consistent and statistically well-defined fit rejection in spite of the strong pixel-noise and gain variations of sCMOS cameras (Fig. 1e,f and Supplementary Note).

Furthermore, to estimate the localization precision, we used the new noise model to compute the Cramér–Rao lower bound, a commonly accepted estimation method of the localization uncertainty ($CRLB_{sCMOS}$) (Supplementary Note). As demonstrated in Fig 1c,d, $CRLB_{sCMOS}$ provides an accurate estimate for localization uncertainty that is achieved by MLE_{sCMOS}.

All described sCMOS-specific algorithms have been implemented in a graphical processor unit environment (GPU; GeForce GTX 690, Nvidia) using Compute Unified Device Architecture (CUDA, Nvidia). This highly parallelized computing technique shortens the analysis time by up to 2–3 orders of magnitude.

Application of our new sCMOS algorithms to the simulated sCMOS data set of two parallel lines described above completely eliminates the artifact observed with conventional algorithms (Fig. 1b). The contributions of high-noise pixels to the signal are statistically de-emphasized in the fitting process (Supplementary Fig. 4). This de-emphasis of a few sparse pixels does not substantially compromise the localization precision in the proximity of these pixels since the signal from every emitter is spread over several pixels. In fact, our algorithm leads to an improved localization performance because the influence of strong noise sources is suppressed (Supplementary Fig. 4) and the correct Maximum Likelihood Estimator is achieved since the appropriate statistics are considered for every pixel. As shown with simulated microtubule images (Supplementary Fig. 5) featuring relatively bright emitters (1,200 detected photons/emitter/frame), we obtain an approximately two-fold resolution improvement with our new algorithms. Moreover, in contrast to conventional MLE, MLE_{sCMOS} achieves its theoretical lower bound of localization precision estimated by $CRLB_{sCMOS}$ at all signal and background levels relevant for practical applications (Fig. 1c,d).

The same phenomena can be observed with experimental data obtained by our custom-built microscope (Supplementary Fig. 6, Online Methods). We imaged microtubules in COS-7 cells immunolabeled with Alexa Fluor 647 (Online Methods) and reconstructed super-resolution images. Artifacts observed when the data was analyzed using conventional algorithms were independent of the imaged sample but correlated with the distribution of

high-noise pixels. Applying our new algorithms completely eliminated these errors (Fig. 1g–k).

Our new algorithms allow to take uncompromised advantage of the superior effective quantum efficiency, readout speed and FOV achievable with sCMOS cameras as compared to EMCCD technology. Calculations based on the CRLB for EMCCDs and $CRLB_{sCMOS}$ for our sCMOS camera show that with the new algorithms, EMCCD cameras achieve better localization precisions only below ~100 detected photons/emitter and negligible background noise (parameters which are usually not achievable in biological applications) (Fig. 1l and Supplementary Fig. 7). For practically relevant parameters and using the new algorithms, our sCMOS camera performs ~12–18% better. Analysis of images of the same 100-nm diameter fluorescent bead imaged first with an EMCCD (Andor iXon 897) and then with our sCMOS camera confirms this theoretical prediction (Supplementary Fig. 8 and Online Methods).

To demonstrate the versatility of our approach, we combined our new algorithms with multi-emitter fitting analysis, which permits unbiased single molecule localization at up to about tenfold higher densities than normally achievable[13] (Supplementary Note). The corresponding reduction in the number of recorded frames combined with the high readout speed of sCMOS cameras allows for substantially faster data acquisition.

We recorded a large FOV (52 × 52 μm^2) super-resolution image of microtubules in COS-7 cells immuno-labeled with Alexa Fluor 647 in 40 s at a frame rate of 400 fps (512 × 512 pixels). More than 4.4 million position estimates (corresponding to a density of ~2,700 estimates per μm fiber length; individual molecules were detected for ~1.47 subsequent frames on average and localized with an average precision of ~14 nm; see Online Methods) resulted in a super-resolution image with ~30–40 nm resolution as confirmed by resolving the two opposite sides of a cylindrical microtubule filament (Fig. 2a–b; Supplementary Data). Recording a smaller 6.6 × 6.6 μm^2 FOV (64 × 64 pixel ROI) made it possible to increase the frame rate to 3,200 fps (Fig. 2e–h). Applying multi-emitter fitting, a reliable super-resolution image could be obtained in only 33 ms, corresponding to 106 recorded camera frames (Fig. 2h). The cost of this speed improvement is an increased localization uncertainty compared to the data in Fig. 2a (Supplementary Fig. 9). However, it represents a critically-important 15–90 fold speed improvement over previously reported high-speed SMSN[7,8,14].

To further demonstrate the feasibility of our approach to high-content screening applications, we imaged the focal adhesion protein Paxillin labeled with Alexa Fluor 647 in a ~26 × 26 μm^2 FOV (256 × 256 pixels) at 800 fps camera frame rate (Fig. 2i–l). In 3 s, a super-resolution image of the Paxillin distribution could be recorded at a density of ~9,000 position estimates/μm^2 (corresponding to an average of one position estimate per 10.5 × 10.5 nm^2; individual molecules were detected for ~1.41 subsequent frames on average and localized with an average precision of ~22 nm; see Online Methods). Assuming a 1-s transition time to move the sample stage between positions, our technique has the potential to record nearly 1,000 different cells per hour and makes the prospect of screening cells by super-resolution imaging a possibility.

To demonstrate live-cell SMSN we chose clathrin-coated structures (CCSs) as an established model system for nanoscopy[7]. We generated a construct encoding clathrin light chain (CLC) fused to the photoswitchable fluorescent protein mEos3.2[15] and transiently transfected it into HeLa cells (Online Methods). Focusing the microscope on the lower (ventral) surface of living cells, we recorded raw data at 600 fps in a FOV of ~26 × 26 μm^2 (256 × 256 pixels; individual molecules were detected for ~1.45 subsequent frames on average and localized with an average precision of ~22 nm; see Online Methods). A super-resolution image based on 34,800 camera frames accumulated in 58 s revealed expected ring-like structures of ~120–150 nm in diameter (Supplementary Fig. 10), representing the axial projection of clathrin-coated pits (CCPs). An elongated appearance of many of these structures was due to motion artifacts as revealed by color-coding the localization estimates by their acquisition time (Fig. 3a,b). In contrast, plotting only data from a 2-s time window, confirms that the clusters are in most cases indeed distributed in ring-like shapes (average localization estimates per CCP per 2-s time window: 211 ± 94 s.d., n = 32; Fig. 3c). Displaying this data as movies (Supplementary Videos 1–5) shows the dynamic lateral motion of CCSs including fission-like events. Strikingly, the ring-shaped structures, indicative of CCPs or nearly completely formed vesicles, often moved in a directed manner at a speed of ~13 nm/s. One explanation for this phenomenon, as previously postulated based on EM images[16], is that growing actin filaments push CCSs away from their point of origin in the process of constriction and elongating the bud neck.

We expanded our studies to a number of other biological test bed systems to show that the instrument can be used to gain new insight about the dynamics of complex shaped organelles, does not perturb cell function and can monitor fast dynamics.

To visualize mitochondrial dynamics, human pyruvate dehydrogenase alpha 1 (PDHA1) was fused to tandem-dimer Eos (tdEos) and imaged in COS-7 cells (Online Methods). A movie reconstructed at 0.5 s temporal resolution (Supplementary Video 6) shows the highly dynamic network and demonstrates the feasibility of sCMOS-based nanoscopy for imaging large, complex objects. Super-resolution imaging of EB3-mEos3.2 in living HeLa cells (Online Methods) shows the growth of microtubule (+) ends at ~120 nm/s (Supplementary Fig. 11 and Supplementary Video 7) which is in good agreement with previously published values[17] and indicates that the used laser intensities do not perturb microtubule polymerization. Additionally, we imaged peroxisome dynamics in COS-7 cells transfected with a peroxisomal membrane protein fused to tdEos (Online Methods). Imaging a FOV of ~26 × 26 μm^2 at 600 fps and collecting the position estimates of 300 frames into single super-resolution images enabled us to record the dynamics of fusion and fission at a temporal resolution of two super-resolution images/s (Fig. 3d–f and Supplementary Videos 8). Without substantial loss of signal, a time course of ~80 s could be imaged corresponding to ~160 reconstructed frames.

The temporal resolution achieved in these live-cell applications is several times higher than any other SMSN of fluorescent proteins previously reported[6,7,18] and even matches the best reported temporal resolution for organic dyes, which are generally much brighter[7].

Next we tested the speed limits of our live-cell imaging approach by using organic dyes and a small FOV to investigate the transient clustering events of transferrin receptors on cell membranes[19]. Transferrin receptors labeled with transferrin-Alexa Fluor 647 (Online Methods) were imaged in a 13 × 13 μm^2 FOV at an acquisition speed of 1,600 fps. Super-resolution images were reconstructed from sequential sets of 50 frames corresponding to a 31 ms acquisition time, or 32 super-resolution images/s (Fig. 4a,b; Supplementary Video 9,10). Super-resolution images at a rate of ~4 images/s failed to resolve fast events such as the transient nature of the receptor clustering and the dynamic movement of the clusters. Video-rate nanoscopy reveals that transferrin receptor cluster sizes are well below the diffraction limit. Additionally, the splitting of single clusters into multiple clusters indicates that the observed clusters consist of multiple receptors. This method complements particle-tracking techniques which can be substantially faster[20] but fail to work reliably at high particle densities and do not provide structural information such as the cluster size and shape. The used buffer and high laser power may raise the concern of damaging cells during the imaging process. However, we did not observe any light-induced changes in cell morphology over the course of imaging in any of our live-cell experiments which is in agreement with previous reports[7]. (Please see Supplementary Note for additional information). Possible long-term effects of SMSN on live samples remain to be investigated.

The new algorithms presented here have unlocked sCMOS technology for unbiased single-molecule localization by accounting for pixel-dependent noise statistically correctly. Importantly, they are not limited to the used sCMOS camera but are readily applicable to any other sCMOS sensor. This provides additional opportunities with even faster and more sensitive cameras being developed. Moreover, our algorithms can be expanded to other detector arrays with non-uniform noise characteristics. The statistical basis of our algorithms is not restricted to particle localization but can be easily expanded to use sCMOS technology in the general field of quantitative image analysis.

The remaining foremost limitation for SMSN is the availability of fluorescent probes, labeling protocols and imaging buffers. Further optimization to increase the specificity of intracellular staining and the signal-to-background ratio in live-cell imaging will expand the application range. The recent progress in this area[8,21–24] makes future breakthroughs highly probable.

While the data presented here has been limited to super-resolution microscopy, our method is equally well applicable to single-particle tracking techniques[25]. The previously achieved temporal resolution of 3.2 kHz in these techniques[20] could be improved sevenfold to ~20 kHz. Moreover, methods which rely on mapping multiple images onto the same camera chip for 3D super-resolution[26,27] or multi-color imaging[28,29] can now benefit from the sCMOS detector's larger FOV, higher quantum efficiency and increased frame rates while achieving localization accuracy and precision at the theoretical limit. The benefits of faster and more sensitive imaging of large FOVs especially pave the way for a new generation of high-throughput nanoscopes.

Online Method

Camera variance, gain and offset calibration

We recorded a series of dark images (60,000 frames) with our sCMOS camera (ORCA-Flash 4.0, Hamamatsu Photonics). The automatic pixel correction which is offered by many sCMOS camera models was disabled for all calibration and application measurements to avoid automatic replacement of high-variance pixels by the average of the neighboring pixels. This correction otherwise prevents correct statistical treatment of the pixel signal. The mean ('offset'), o_i, and the variance, var_i, for each pixel i were calculated by temporal mean and variance operations over the acquired dark frames. The amplification gain, g_i, for each pixel was estimated from 15 sets of 20,000 frames each which were recorded at different illumination intensities ranging from approximately 20 to 200 photons per pixel (Supplementary Note).

Simulations of super-resolution sCMOS datasets

For the simulated line pattern, single emitters were simulated using a pixel-integrated symmetric two-dimensional (2D) Gaussian model[13]. The switching behavior was simulated using a Markov model with k_{off} (bright to dark) and k_{on} (dark to bright) rates of 0.8 frame^{-1} and 10^{-5} frame^{-1}, respectively. These rates were chosen to ensure non-overlapping emitters. Single emitters were simulated with 200 photons per molecule incident on the camera, 5 photons detected per pixel as the background, a 2D Gaussian-shaped point-spread function (PSF) with 133 nm standard deviation, 75% camera quantum efficiency and a pixel size of 103 nm to match our experimental setup. Images of the simulated structure of two lines with 80 nm distance were generated first with Poisson noise and then pixel-dependent Gaussian noise was added to each pixel in the simulated sub-region where the variance, offset and gain values of each pixel had been obtained from a sub-region of our sCMOS camera. This noise mapping method ensures realistic simulation of sCMOS noise behavior.

Generation of goodness of fit metric (LLR) histograms (Fig. 1e,f)

10,000 7 × 7 pixel sub-regions each with a single emitter (200 total incident photons from single molecule and 5 background photons per pixel) were simulated separately in two different sub-regions. Noise was added to the images using the noise mapping method described above. Localization analysis was performed using MLE and MLE_{sCMOS}, respectively, and LLR and LLR_{sCMOS} were calculated.. The χ^2 distribution with 45 degrees of freedom (number of pixels – number of fit parameters)[30] is plotted in Fig. 1e,f.

Comparison of MLE-results with CRLB (Fig. 1c,d)

At each incident photon level, simulations were performed at 1,000 randomly distributed positions using the noise mapping method. In each sub-region, 1,000 single emitters were simulated and fit by MLE and MLE_{sCMOS}, respectively. The localization uncertainty is the standard deviation of the localization estimates. The distribution of these values over the 1,000 sub-regions then provides a mean localization uncertainty and its standard deviation. The CRLB and $CRLB_{sCMOS}$ were determined as the mean value of the CRLBs calculated

from the localization estimates of all 1,000 × 1,000 simulations for each signal photon/background combination for the conventional method and sCMOS method, respectively.

Imaging of fluorescent beads and single-molecule analysis

A sample of 100 nm fluorescent beads (F-8801, Life Technologies) was prepared on a coverslip and imaged with our custom-built microscope (Supplementary Fig. 6) using a 63×/1.2 NA water immersion objective (C-Apochromat 63×/1.2 W Corr, Zeiss). The effective pixel sizes were matched between the two cameras for fair comparison using relay lenses (pixel size in the sample plane: 101 nm for EMCCD and 103 nm for sCMOS). A mirror on a magnetic retention base enabled fast switching between the two cameras with minimal disturbance to the imaging system. A 568 nm laser (Innova 300, Coherent) was used at a low intensity (~0.1 mW measured before the objective) as excitation source. Images were taken first with the EMCCD and then the sCMOS camera to rule out a decrease in localization precision caused by photobleaching. Photobleaching was not observed over the acquisition period (data not shown). Datasets from EMCCD and sCMOS datasets (800 frames each), were analyzed using MLE[12] and MLE_{sCMOS} (Supplementary Note), respectively.

Plasmid construction

The Human Paxillin sequence (NM_002859.2) was amplified using polymerase chain reaction (PCR) and cloned into the pCMV-3TAG 1A vector (Agilent Technologies, USA) to obtain a construct expressing an N-terminal FLAG-tagged version of Paxillin.

mEos3.2 and tdEos fluorescent protein (FP) expression vectors were constructed using C1 and N1 (Clontech™-style) cloning vectors. The FP cDNAs were amplified with a 5′ primer encoding an AgeI site and a 3′ primer encoding a NotI site (N1) or a BspEI site (C1) for insertion into the appropriate cloning vector backbone. The PCR products and EGFP-C1 and -N1 cloning vectors were gel-purified and digested with the appropriate enzymes prior to ligation to generate new cloning vectors with the Eos FP coding regions. All fusions were first constructed using an EGFP variant with mutations designed to enhance folding (mEmerald), which is well-behaved with respect to monomeric character and lack of localization artifacts. These vectors served as pilots to demonstrate proper localization of constructs to confirm the performance of the photoconvertable FPs. Thus, an N-terminal fusion (with respect to the targeting protein) was constructed to produce a human clathrin light chain (CLC) fusion (NM_001834.2; a gift from G. Patterson, NIH) with a 15 amino acid linker separating the fluorescent protein from clathrin. CLC cDNA was amplified using the primers listed in the Supplementary Table. The resulting PCR product and mEmerald-C1 cloning vector were digested with the appropriate restriction enzymes and the products were ligated to yield mEmerald-CLC. The same process was also utilized to generate human EB3 (NM_012326.2; Origene) using the primers listed in the Supplementary Table. The PCR product and mEmerald-C1 were digested by the appropriate enzymes and ligated to yield mEmerald-EB3 with an 18-amino acid linker separating the proteins. In both cases after proper localization was confirmed, mEos3.2 was substituted for mEmerald by digesting with BglII and NheI enzymes. This yielded mEos3.2-CLC and mEos3.2-EB3.

To produce a pilot C-terminal fusion (with respect to the targeting protein), human peroxisomal membrane protein (PMP) (NM_018663.1; Origene) was amplified using the primers listed in the Supplementary Table. The resulting PCR product and mEmerald-N1 were digested by the appropriate restriction enzymes and the products were ligated to yield PMP-mEmerald with a 10-amino acid linker separating the proteins. After confirmation of proper localization, the resulting construct and tdEos-N1 were then sequentially digested with AgeI and NotI and ligated to form PMP-tdEos.

In a similar manner, human pyruvate dehydrogenase alpha 1 (PDHA1) (NM_000284.3; Origene) was amplified using the primers listed in the Supplementary Table. The PCR product and mEmerald-N1 were digested by the appropriate enzymes and ligated to yield PDHA1-mEmerald with a 10-amino acid linker separating the proteins. Subsequent to confirming proper localization, the resulting construct and tdEos-N1 were then digested with BamHI and NotI and ligated together to form PDHA1-tdEos.

The DNA used for transfection was prepared using the Plasmid Maxi kit (QIAGEN). To ensure proper localization, mEos3.2 and tdEos fusion proteins were characterized by transfection in HeLa cells (CCL2 line; ATCC) using Effectene (QIAGEN) and ~1μg vector. Transfected cells were grown on coverslips in DMEM/F12, fixed after 48 hours, and mounted with Gelvatol.

Sample preparation for microtubule imaging

COS-7 cells (ATCC) were grown in DMEM/F12 (Invitrogen) supplemented with 2mM L-glutamine (Gibco), 10% Fetal Bovine Serum (FBS, ATCC) and 1% Penicillin (10,000 IU/mL)/Streptomycin (10,000 μg/mL) (P/S, ATCC) at 37°C with 5% CO_2. Prior to imaging, cells were grown in 35 mm dishes on #1.5 glass cover slips pre-coated with poly-L-lysine (MatTek) and fibronectin. To label microtubules, cells were washed three times with PBS pre-warmed to 37°C and pre-extracted with 0.2% saponin (Sigma) in Cytoskeleton Buffer (CSB, 10 mM MES pH 6.1 (Sigma), 150 mM NaCl, 5 mM $MgCl_2$ (Sigma), 5 mM EGTA (Sigma), 5 mM glucose) for 1 min at room temperature. After aspirating the solution, the cells were fixed with 3% paraformaldehyde (PFA, Electron Microscopy Sciences) and 0.1% glutaraldehyde (Electron Microscopy Sciences) diluted in CBS for 15 min. Cells were washed three times for 3-min intervals with PBS and then permeabilized and blocked with blocking buffer (3% BSA (Sigma) and 0.2% TX-100 in PBS) for 30 minutes while gently rocking. The buffer was aspirated and the cells were incubated with mouse monoclonal anti-α-tubulin antibody (Sigma, 1:1,000 dilution) at room temperature for 1 h. Cells were washed three times for 3-min intervals using wash buffer (WB; 0.05% TX-100 in PBS) and incubated with Alexa Fluor 647 goat anti-mouse IgG (Invitrogen) at a concentration of approximately 5 μg/mL for 1 h. Cells were washed with the WB for three 3-min intervals and post-fixed with 3% PFA and 0.1% glutaraldehyde diluted in CSB for 10 min. Samples were washed three times in PBS for 3-min intervals and stored in PBS at 4°C until imaging.

Sample preparation for focal adhesion imaging

2×10^5 HeLa cells grown in DMEM (Invitrogen) with 10% FBS were seeded on a 35 mm glass bottom dish (MatTek corporation; No. 1.5 coverglass). After overnight incubation, the

cells were transfected with 500 ng of plasmid DNA expressing N-terminal FLAG tagged focal adhesion marker Paxillin using FuGENE HD transfection reagent (Promega Inc; E2311). 24 h post transfection the cells were fixed with 4 % paraformaldehyde (PFA) and processed for immunofluorescence. Briefly, the cells were permeabilized with 0.5% Triton-X-100, treated with monoclonal antibodies to FLAG epitope (1:1000 dilution, Clone M2, Sigma-Aldrich; F3165; 1 mg/ml) in phosphate buffered saline containing 3% Bovine serum albumin Fraction V (American Bioanalytical, Inc; AB01088). This was followed by treatment with Alexa Fluor 647 conjugated goat secondary antibodies to mouse (1:2000 dilution; Invitrogen; A-21236; 2 mg/ml). The cells were then post-fixed with 4% PFA. Immediately before image acquisition, the cells were mounted in STORM-imaging buffer and overlaid with mineral oil.

Sample preparation for live cell imaging with photoswitchable fluorescent proteins

HeLa and COS-7 cells were grown in DMEM (high glucose, phenol red-free, Invitrogen) supplemented with 10% FBS and 1% P/S were seeded on a 35 mm glass bottom dish (MatTek; #1.5 cover glass). After overnight incubation, the cells were transfected with 2 μg of plasmids using FuGENE HD transfection reagent (Promega). Cells were washed with supplemented media 24 h post transfection, and incubated overnight. Before imaging, the cells were washed with supplemented growing media.

Sample preparation for live-cell imaging of transferring

EA.hy926 cells were grown in DMEM (high glucose, phenol red-free, Invitrogen) supplemented with 10% FBS and 1% P/S at 37°C with 5% CO_2. Prior to imaging, cells were grown in 35 mm dishes with #1.5 glass cover slips coated with Collagen (MatTek). One hour prior to labeling, EA.hy926 cells were incubated in DMEM (high glucose, phenol red free) without serum. Transferrin from human serum, conjugated to Alexa Fluor 647 (Life Technologies) was reconstituted with deionized water to a concentration of 5 mg/mL and stored at 4°C. The transferrin Alexa Fluor 647 conjugate was diluted to 10 μg/mL in DMEM (high glucose, phenol red-free), and incubated with EA.hy926 cells for 45 min. After labeling, cells were washed three times with 1× PBS. To remove transferrin-Alexa Fluor 647 bound to the plasma membrane, cells were washed once with 50 mM MES, pH 5.0,150 mM NaCl and twice with 1× PBS. Cells were imaged in 1 mL of DMEM (high glucose, phenol red free) supplemented with 25 μM 2-ME, 10 μL of glucose oxidase and 4 μL of catalase at room temperature.

Imaging buffer preparation for Alexa Fluor 647-labeled samples

Oxygen scavenging enzymes, 1 kU/mL catalase from bovine liver (Sigma) and 0.135 kU/ml glucose oxidase from *Aspergillus niger* (Sigma), were reconstituted in 20 mM Tris pH 7.4 (Sigma), 50 mM NaCl (Sigma) and 28.4 mM 2-mercaptoethanol (2-ME, Sigma). Oxygen scavenging enzymes were stored separately in 50% glycerol at −20°C at concentrations of 500 kU/mL of catalase and 13.5 kU/mL of glucose oxidase. Oxygen scavenging enzymes were diluted into imaging buffer (50 mM Tris, pH 8.0, 50 mM NaCl (Sigma), 10% glucose) immediately before use. For imaging, 20 μL of glucose oxidase and 4 μL of catalase stocks were added to 1 mL of 1% (v/v) 2-ME in imaging buffer.

Imaging of fixed and live cells

All biological images were recorded on a custom-built setup (Supplementary Fig. 6) based on a commercial microscope stand (Axio Observer D1, Carl Zeiss MicroImaging) with a 100×/1.46 NA oil immersion objective (alpha Plan-Apochromat 100×/1.46 Oil, Zeiss). The setup is equipped with lasers emitting at 405 nm (CrystaLaser, 50 mW), 568 nm (Coherent Innova 300, ~400 mW) and 642 nm (MPB Communications, 500 mW). Fluorescence was recorded by our sCMOS camera through the side port of the stand. All data was recorded at room temperature.

Fixed microtubule structures were imaged in a 128 × 128 pixel ROI for 40,000 frames at 1,600 fps (Fig. 1g–k), a 512 × 512 pixel ROI for 16,000 frames at 400 fps (Fig. 2a,b) and a 64 × 64 pixel ROI for 30,000 frames at 3,200 fps (Fig. 2e–h). The 642 nm laser was used at intensities of 18.4 kW/cm^2, 5.5 kW/cm^2, and 7.4 kW/cm^2, respectively. Images were acquired using HCimage software (Hamamatsu). Focal adhesions were recorded in a 256 × 256 pixel ROI for 2,400 frames at 800 fps with the 642 nm laser intensity set to 9.2 kW/cm^2. Clathrin data was recorded in a 256 × 256 pixel ROI for 50,000 frames at 600 fps with the 568 nm laser intensity set to 5.3 kW/cm^2. Mitochondria were recorded in a 256 × 256 pixel ROI for 80,000 frames at 400 fps with the 568 nm laser intensity set to 5.3 kW/cm^2. EB3 data was recorded in a 256 × 256 pixel ROI for 30,000 frames at 600 fps with the 568 nm laser intensity set to 5.3 kW/cm^2. Peroxisomes were recorded in a 256 × 256 pixel ROI for 50,000 frames at 600 fps with the 568 nm laser intensity set to 5.3 kW/cm^2. Transferrin data was recorded in a 128 × 128 pixel ROI at 1,600 fps with the 642 nm laser intensity set to 7.4 kW/cm^2. During imaging, the intensity of the 405 nm activation laser was manually increased from 0 to 0.3 W/cm^2 (for 512 × 512 pixel ROI) and 0 to 1.8 W/cm^2 (for 256 × 256, 128 × 128 and 64 × 64 pixel ROI) to ensure optimal particle densities for either single emitter fitting or multi-emitter fitting[31].

Super-resolution analysis and reconstruction for fixed and live cell experiments

For the conventional MLE method, raw images recorded with the sCMOS camera were first Poisson-calibrated[13] by subtracting a pre-determined offset value and then dividing by a constant gain factor (provided by the manufacturer)[13,32]. The calibrated images were then analyzed using the conventional MLE method. The fit parameters were: the emitter position (x, y), the number of detected photons, and the background value. The localization precision was estimated by the conventional CRLB. Finally, super-resolution images were reconstructed by plotting pixel-integrated 2D Gaussians[13] at each localized position, each with standard deviations in the x and y directions equal to the corresponding CRLB estimates of localization uncertainties.

For the sCMOS-specific method, particles were identified and segmented in the raw sCMOS images using IS_{sCMOS} (Supplementary Note), and then fitted using MLE_{sCMOS}.The localization precision was estimated by $CRLB_{sCMOS}$. Super-resolution images for Fig. 1 were reconstructed as described above for conventional MLE.

To obtain the super-resolution images shown in Fig. 2–4, only the sCMOS-specific algorithms were used. In Fig. 2a–b and Fig. 3 single-emitter analysis was performed and

localization results were filtered using LLR_{sCMOS}. For reconstruction, localization estimates were binned into a 2D histogram image. The value of each pixel indicates the number of localization estimates in the pixel. The pixel size in the 2D histogram images shown was 5.15 nm in Fig. 2a–b, 10.3 nm in Fig 3a–c and 20.6 nm in Fig. 3d–f. To aid visualization, each image was convolved with a 2D Gaussian kernel with σ = 1.5 pixels for Fig. 2a–b and 1 pixel for Fig. 3.

In Fig. 2e–l and Fig. 4, multi-emitter fitting was performed using the fitting parameters: position (*x*, *y*), effective photon count and background. Initial guesses of effective photon count were 250 (Fig. 2e–h), 350 (Fig. 2i–l) and 200 (Fig. 4). For all datasets, the maximal number of emitter models fitted within a single sub-region was set to 4 and the sigma of the Gaussian emitter model was set to 133 nm. A p-value of 10^{-10} from the LLR_{sCMOS} was used as the rejection threshold. To reconstruct the super-resolution image, localization estimates from the remaining particles were binned into a 2D histogram image with 10.3 nm pixel size. To aid visualization each resulting image was convolved with a 2D Gaussian kernel with σ = 1 pixel (Fig. 2e–l) and 2 pixels (Fig. 4).

To provide an estimate for the average number of consecutive frames over which single molecules were detected, localization events were considered to stem from the same molecule if located within a radius of 3-times the localization uncertainty.

The software code is available for academic use on request from the authors.

Generation of difference images (Fig. 1j,k)

After localization using MLE or MLE_{sCMOS}, 2D histogram images were generated with 10.3 nm pixel size. The difference image was obtained by subtracting the MLE_{sCMOS} image from the conventional MLE image. To aid visualization, the resulting images were convolved with a 2D Gaussian kernel (σ = 2 pixels).

Tracking of EB3 and clathrin coated pits

The series of EB3 super-resolution images was imported in Velocity 6.2 (Velocity Medical Solutions) and the tips of the growing microtubules were tracked using the manual tracking mode. For the series of super-resolution CCP images, the centers of identified CCP were tracked manually in MATLAB during the individual periods of directed movement (5–20 s).

Emitter density calculation

To estimate the number of localized emitters per area in Fig. 2, we extracted the number of localization estimates from a representative 1 μm segment of straight microtubule using an integration width of 80 nm (Fig. 2a,b). For the Paxillin data, estimates were counted in a 240 × 240 nm^2 square box centered on a large focal adhesion (Fig. 2j). The 1D and 2D localization densities were calculated as the number of localization estimators determined per length unit and per area unit respectively.

Nyquist resolution measurement

To estimate the Nyquist resolution in Fig. 4a,b, we first determined masks covering the area of each transferrin cluster in each super-resolution image. Determining the number of localization estimates in the clusters and dividing it by the cluster area yielded the localization density. The Nyquist resolution was calculated for the 2D case[7] as $2/(\text{localization density})^{1/2}$.

Supplementary Material

Refer to Web version on PubMed Central for supplementary material.

ACKNOWLEDGEMENTS

We thank J. Munro, P. Pellett, L. Schroeder, F. Bottanelli (Yale University) and M. Gudheti (Vutara, Inc.) for helpful discussions about the buffer and sample preparation, J. Spatz (Max Planck Institute for Intelligent Systems) for support and P. de Camilli, O. Idevall-Hagren, T. Gould, E. Allgeyer and E. Kromann (Yale University) for helpful comments on the manuscript. We thank P. Xu (Chinese Academy of Sciences) for providing the mEos3.2 plasmid for initial experiments. This work was supported by grants from the Wellcome Trust (095927/A/11/Z), the National Institutes of Health (R01 CA098727; to W.M) and the Raymond and Beverly Sackler Institute for Biological, Physical and Engineering Sciences.

REFERENCES

1. Hell SW. Nat. Methods. 2009; 6:24–32. [PubMed: 19116611]
2. Gould TJ, Hess ST, Bewersdorf J. Annu. Rev. Biomed. Eng. 2012; 14:231–254. [PubMed: 22559319]
3. Van de Linde S, Heilemann M, Sauer M. Annu. Rev. Phys. Chem. 2012; 63:519–540. [PubMed: 22404589]
4. Mortensen KI, Churchman LS, Spudich JA, Flyvbjerg H. Nat. Methods. 2010; 7:377–381. [PubMed: 20364147]
5. Chao J, Ram S, Ward ES, Ober RJ. Nat. Methods. 2013; 10:335–338. [PubMed: 23455923]
6. Hess ST, et al. Proc. Natl. Acad. Sci. USA. 2007; 104:17370–17375. [PubMed: 17959773]
7. Jones SA, Shim S-H, He J, Zhuang X. Fast. Nat. Methods. 2011; 8:499–505. [PubMed: 21552254]
8. Shim S-H, et al. Proc. Natl. Acad. Sci. USA. 2012; 109:13978–13983. [PubMed: 22891300]
9. Saurabh S, Maji S, Bruchez MP. Opt. Express. 2012; 20:7338–7349. [PubMed: 22453414]
10. Long F, Zeng S, Huang Z-L. Opt. Express. 2012; 20:17741–17759. [PubMed: 23038326]
11. Ober RJ, Ram S, Ward ES. Biophys. J. 2004; 86:1185–1200. [PubMed: 14747353]
12. Smith CS, Joseph N, Rieger B, Lidke KA. Nat. Methods. 2010; 7:373–375. [PubMed: 20364146]
13. Huang F, Schwartz SL, Byars JM, Lidke KA. Biomed. Opt. Express. 2011; 2:1377–1393. [PubMed: 21559149]
14. Zhu L, Zhang W, Elnatan D, Huang B. Nat. Methods. 2012; 9:721–723. [PubMed: 22522657]
15. Zhang M, et al. Nat. Methods. 2012; 9:727–729. [PubMed: 22581370]
16. Collins A, Warrington A, Taylor KA, Svitkina T. Curr. Biol. 2011; 21:1167–1175. [PubMed: 21723126]
17. Sironi L, et al. Cytoskeleton (Hoboken). 2011; 68:266–278. [PubMed: 21491614]
18. Biteen JS, Goley ED, Shapiro L, Moerner WE. Chemphyschem. 2012; 13:1007–1012. [PubMed: 22262316]
19. Doherty GJ, McMahon HT. Annu. Rev. Biochem. 2009; 78:857–902. [PubMed: 19317650]
20. Juette MF, Bewersdorf J. Nano Lett. 2010; 10:4657–4663. [PubMed: 20939601]
21. Lukinavičius G, et al. Nat. Chem. 2013; 5:132–139. [PubMed: 23344448]
22. Benke A, Manley S. Chembiochem. 2012; 13:298–301. [PubMed: 22213360]

23. Vaughan JC, Jia S, Zhuang X. Nat. Methods. 2012; 9:1181–1184. [PubMed: 23103881]
24. Lee MK, Williams J, Twieg RJ, Rao J, Moerner WE. Chem. Sci. 2013; 4:220–225. [PubMed: 23894694]
25. Manley S, et al. Nat. Methods. 2008; 5:155–157. [PubMed: 18193054]
26. Juette MF, et al. Nat. Methods. 2008; 5:527–529. [PubMed: 18469823]
27. Aquino D, et al. Nat. Methods. 2011; 8:353–359. [PubMed: 21399636]
28. Testa I, et al. Biophys. J. 2010; 99:2686–2694. [PubMed: 20959110]
29. Gunewardene MS, et al. Biophys. J. 2011; 101:1522–1528. [PubMed: 21943434]
30. Wilks SS. Ann. Math. Statist. 1938; 9:60–62.
31. Shore E, Small A. Opt. Lett. 2011; 36:289–291. [PubMed: 21263529]
32. Lidke KA, Rieger B, Lidke DS, Jovin TM. IEEE Trans. Image Process. 2005; 14:1237–1245. [PubMed: 16190460]

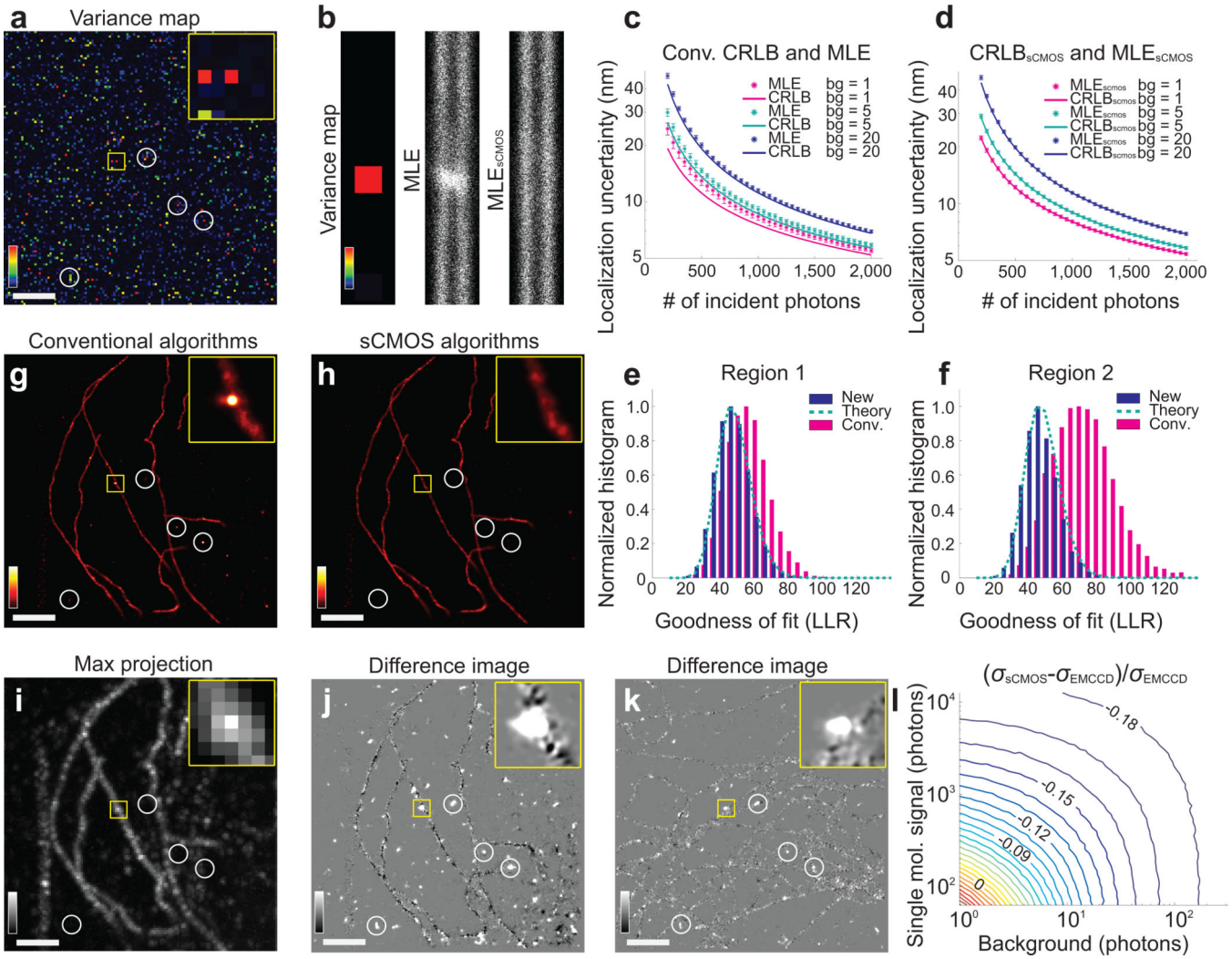

Fig. 1.

sCMOS camera specific algorithms enable unbiased SMSN at the theoretical limit. (**a**) Readout variance map of a 128 × 128 pixel region in the center of a sCMOS camera. (**b**) Simulation of single emitters on a parallel line pair based on the shown variance map and localized using conventional MLE and MLE$_{sCMOS}$. (**c, d**) Uncertainty estimator performance comparison for sCMOS camera data between conventional MLE and CRLB (**c**) and between MLE$_{sCMOS}$ and CRLB$_{sCMOS}$ (**d**) for different detected background photon values/pixel (bg) and single-molecule photon numbers incident on the camera chip. (**e, f**) Comparison of LLR, LLR$_{sCMOS}$ and the theoretically predicted distribution for two different locations on the camera chip. (**g, h**) Reconstructed super-resolution images of microtubules analyzed using conventional (**g**) and sCMOS algorithms (**h**). (**i**) Maximum projection of raw data used for (**g, h**) representing the diffraction-limited image. (**j**) Difference images of (**g**) and (**h**). Zero differences are shown in gray. (**k**) Difference image of another microtubule data set recorded in the same camera region. Artifacts in (**g, j, k**) correlate with high-noise pixels in (**a**) as highlighted by the white circles. The yellow boxes in (**a, g–k**) denote the positions of the enlarged sections shown in the insets. (**l**) Relative improvement in

localization precision predicted by CRLB for EMCCD cameras and $CRLB_{sCMOS}$ for sCMOS, respectively. Color bars: (**a, b**) 0–400 ADU^2; (**i**) min-max signal; (**g, h**) normalized to same scale; (**j, k**) normalized to same scale. Scale bar in (**a, g–k**): 2 μm.

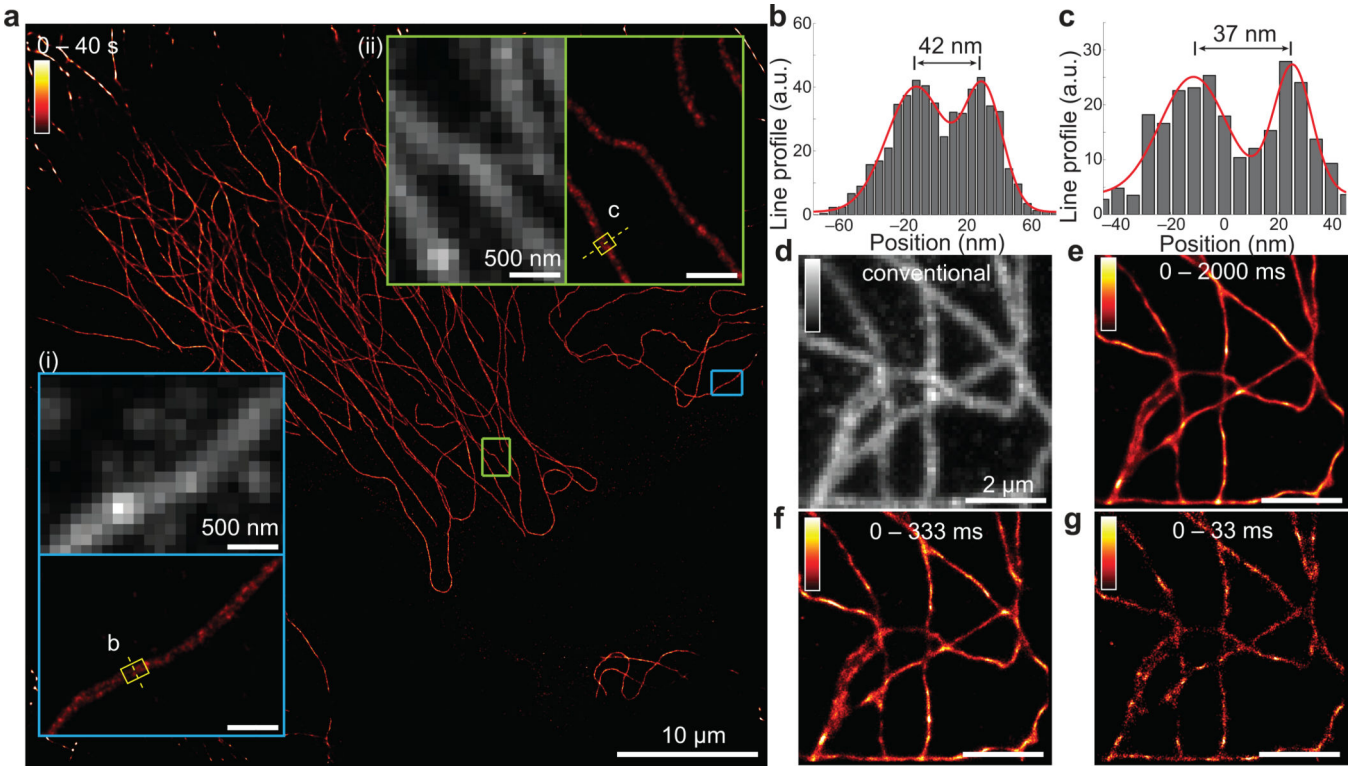

Fig. 2.

Unbiased, fast SMSN of fixed microtubules and focal adhesions demonstrating high-throughput capabilities. (**a**) Super-resolution image of microtubules in a 53 × 53 µm^2 ROI imaged at 400 fps in 40 s. The data set was processed by the new sCMOS-specific algorithm resulting in about 4.4 million position estimates after filtering. The area marked by the blue box is shown in the inset as a maximum projection of the raw data (entire analyzed data set) representing the diffraction-limited wide-field image and as the super-resolution image. For visualization purposes, the upper bound in the color table has been adjusted for the overview image. (**b**) Enlarged maximum projection of raw data and super-resolution image of the area highlighted by the green box in (**a**). (**c,d**) Line profiles of position estimates in the small yellow boxes shown in (**a**) and (**b**), respectively. (**e**) Maximum projection of a microtubule raw data set recorded in a 6.5 × 6.5 µm^2 FOV at 3,200 fps in 2 s total. (**f–h**) Reconstructed super-resolution images obtained from different subsets of the same raw data stack using sCMOS-specific multi-emitter fitting. (**i,j**) Maximum projection of a data set showing the distribution of Paxillin in focal adhesions recorded in 3 s and the corresponding super-resolution image, respectively. (**k**) Enlarged display of the area marked by the white boxes in (**i,j**). (**l**) Profile displaying the distribution of position estimates in the yellow box shown in the super-resolution image in (**k**).

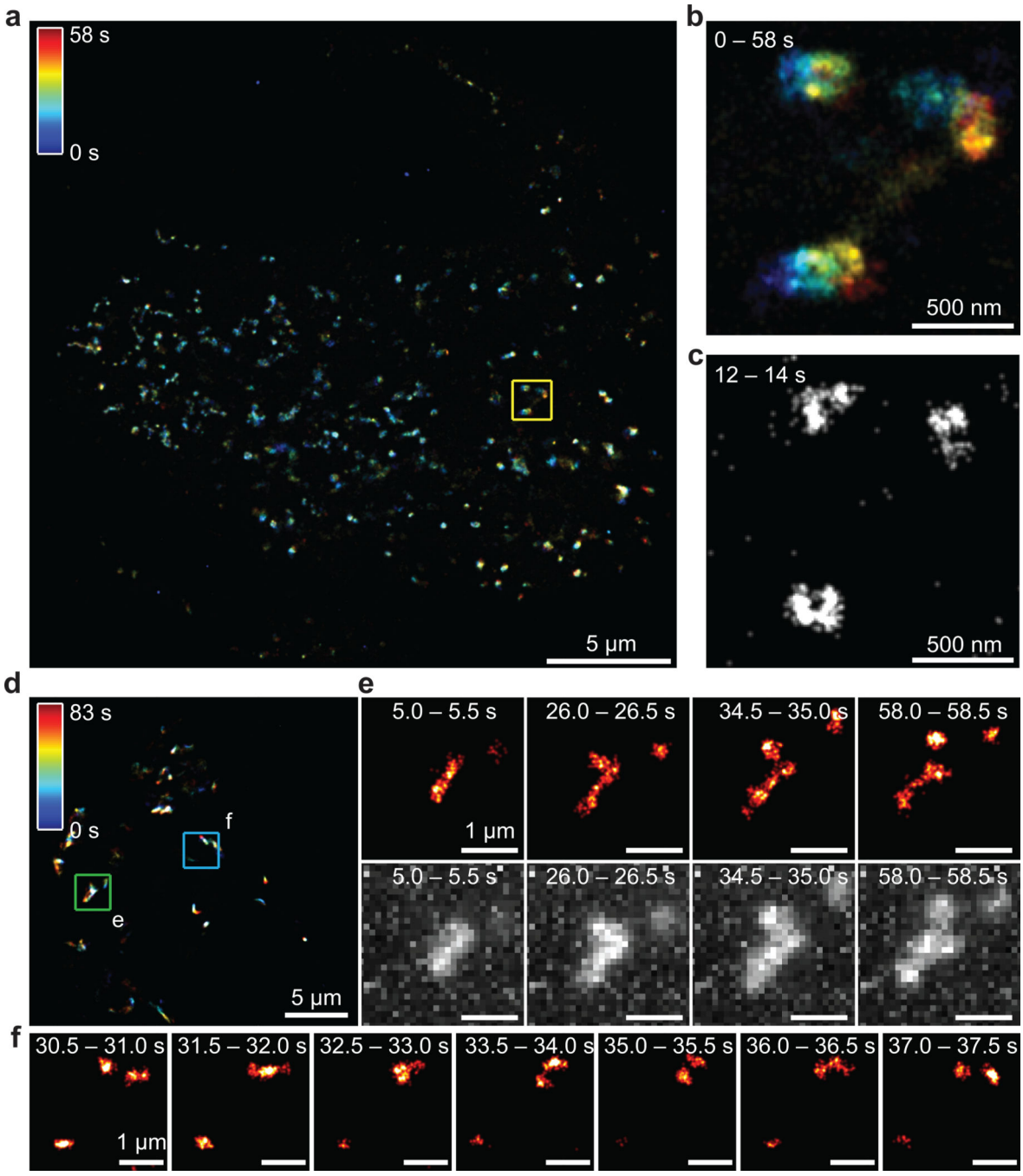

Fig. 3.

Live-cell SMSN at 0.5 to 2 s temporal resolution. (**a**) Super-resolution image of mEos3.2-labeled clathrin-coated pits (CCPs) in a live HeLa cell. The localization estimates are colored according to their recording time. (**b**) The enlarged image of the area marked by the yellow box in (**a**) reveals that movements of the structures over the course of recording obscure the details in the image. (**c**) Rings representing axial projections of CCPs can be resolved when displaying only a 2-s time window of the data. (**d–f**) Peroxisome dynamics in a live COS-7 cell labeled by tdEos. (**d**) Overview image of an 83-s data set. Data has been

colored analogous to (**a**). (**e**) Super-resolution images and maximum projections of the raw data from the area in the green box in (**d**) in short 0.5-s time intervals. (**f**) Super-resolution images at 0.5-s time resolution of the area highlighted by the blue box in (**d**). Only every second frame is shown. See also Supplementary Fig. 10 and Supplementary Videos 1–5, 8 and 9.

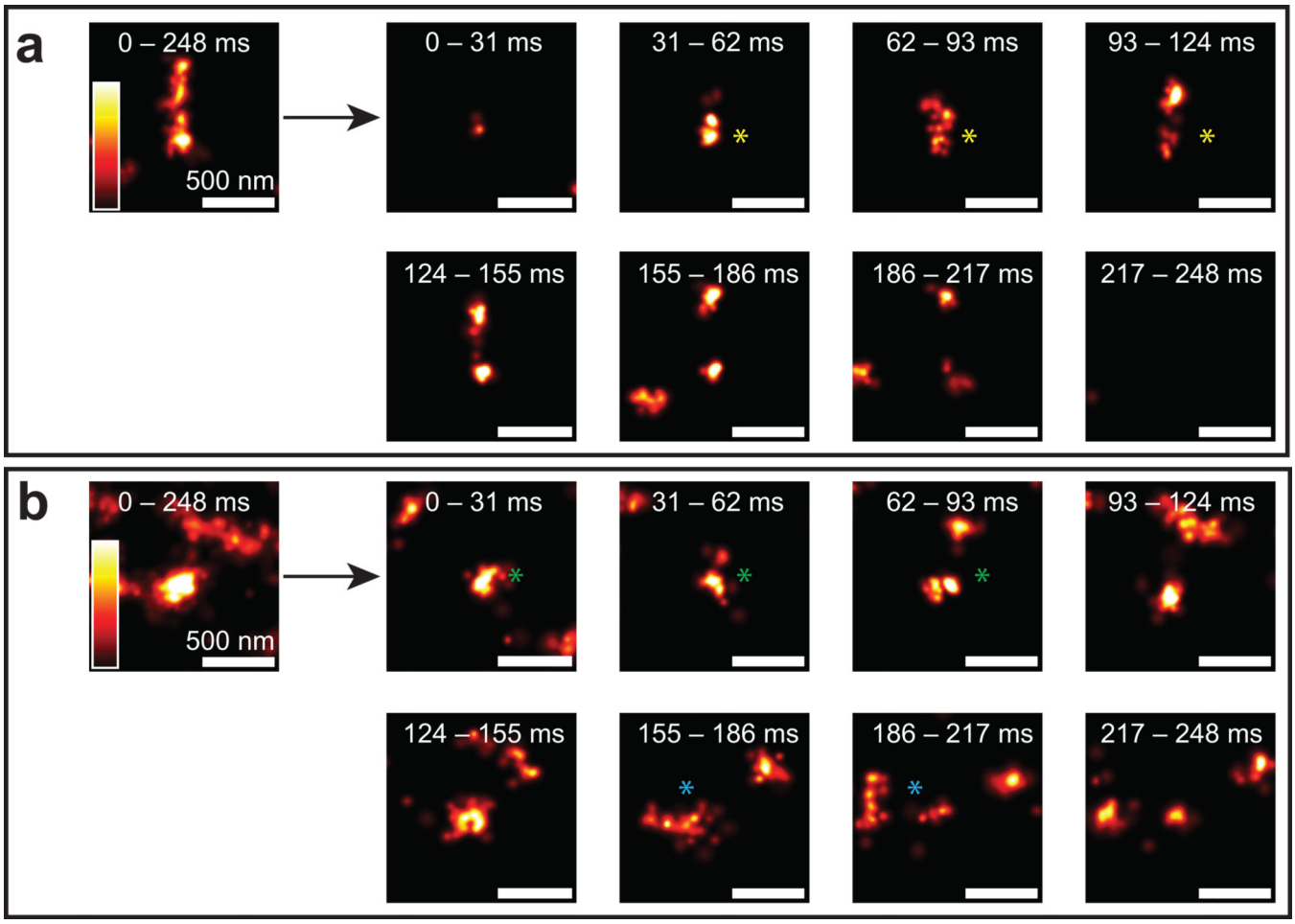

Fig. 4.

Video-rate live-cell nanoscopy of transferrin receptor clusters in live EA.hy926 cells. (**a–b**) Two examples of super-resolved transferrin cluster dynamics from a larger data set. Asterisks show splitting of single clusters into multiple clusters. Super-resolution images at a slower rate (~4 super-resolution images/s; shown on the left) lead to artifactual structures due to diffusion as visualized by reconstructed sequences of the same data at higher frame rates (~32 super-resolution images/s; on the right).